

Identifying Potentially Activatable Faults for the Appalachian Basin Geothermal Play Fairway Analysis

Frank Horowitz

18-September-2015

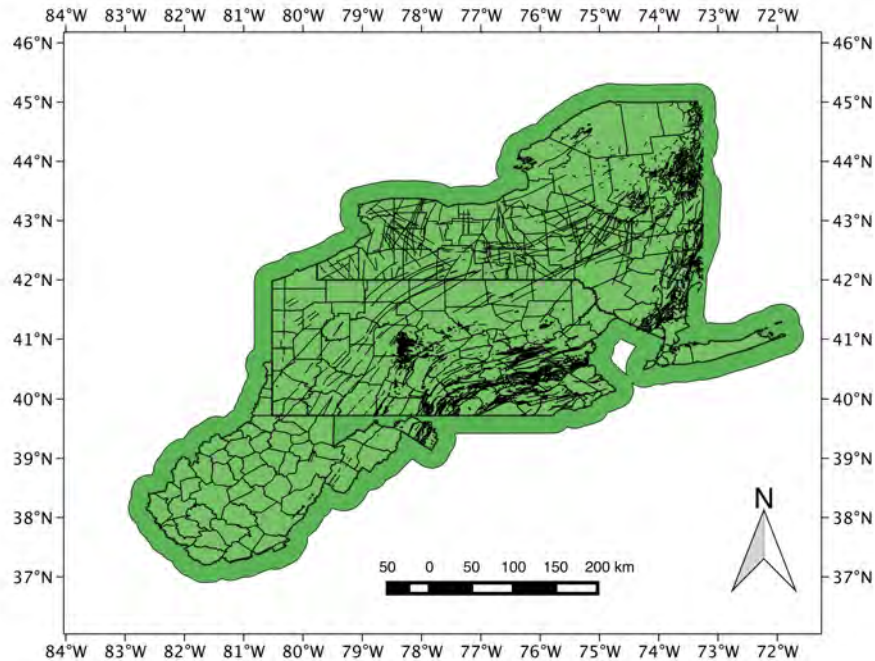


Figure 1: Mapped faults and other lineaments available in GIS form on the GPFA-AB server. Note the uneven regional coverage and un-geological artifacts such as state-boundary truncations of structures.

Existing fault maps (Figure 1) do not share the Appalachian Basin Geothermal Play Fairway Analysis (GPFA-AB) boundaries or scale. Hence, their use leads to problems of uneven coverage, varying interpretation of faults vs. lineaments, and different mapping scales. For more uniformity across the GPFA-AB region, we use an analysis of gravity and magnetic fields discussed next.

In order to provide a spatially uniform coverage of candidate faults, I turned to the Poisson wavelet multi-scale edge analysis of potential fields – informally known for brevity as the ‘worm’ technique – my co-workers and I developed starting nearly 20 years ago: Hornby et al. (1999) (independently derived by Moreau et al., 1997). This technique, widely deployed in the mining community in Australia and elsewhere (e.g. GoldCorp, 2001), uses gravity and magnetic fields to detect lateral contrasts in mass density or magnetization strength respectively. Figure 2 displays a cartoon summary of the technique.

Some theoretical advantages of the technique include:

- Marrying wavelet theory and potential field physics by building a wavelet from the Green’s function of the Poisson equation (Laplace’s equation with sources).
- The inverse wavelet transform has a physical interpretation as an *induced* inversion to a dipole source distribution (Boschetti et al., 2001; Hornby et al., 2002) that produces a field that is exactly the starting field. The regularizing assumption is that ‘Rocks Have Edges’.
- The field values at the locations of the multiscale edges (worms) alone, when combined with the inverse wavelet transform above, produce a field that is a close approximation of the starting field via

Physical Interpretation of the Worms (Induced Inversion)

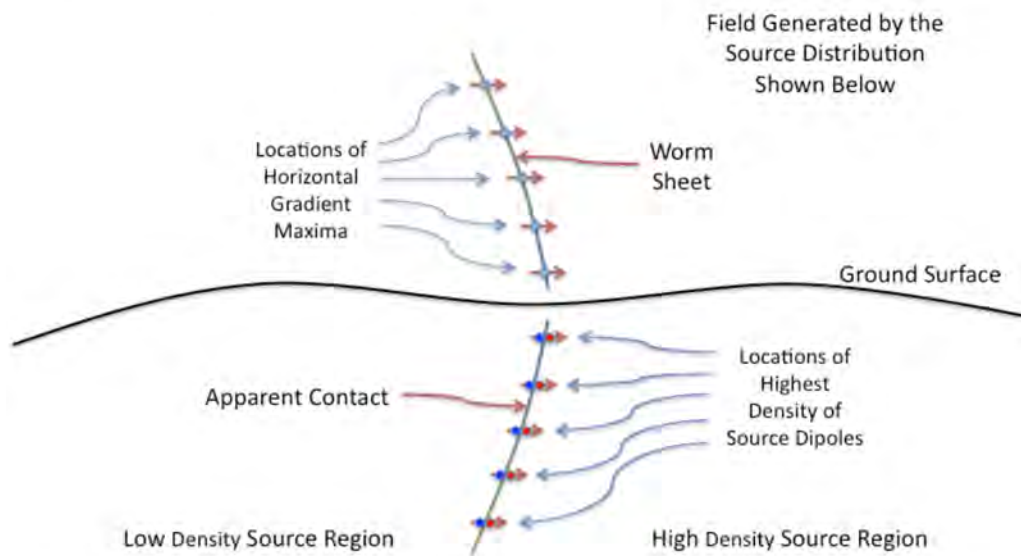


Figure 2: A vertical cross-section cartoon of the worm technique. The gravity or magnetic field is notionally known completely at the ground surface. The field is upward continued to a suite of heights. Hornby et al. (1999) show that each level of upward continuation corresponds to a (continuous) wavelet scale. The locations of maxima in the horizontal gradient of the field at each height become an edge (or a 'worm') for the corresponding scale (the intersection of these 1D features with the plane of section are shown as blue dots above ground), the collection of edges at all scales are 'multiscale edges'. A suite of worms arising from connected locations on the ground is a 'worm sheet'. As explained in the text, an underground inversion is induced via a physical interpretation of the inverse wavelet transform as a distribution of dipole sources. Draping the worm sheets underground (blue and red dots) results in a visualization of the locations of highest density of dipole sources. These are interpreted as the locations of apparent lateral contacts.

the result from Mallat and Zhong (1992).

Hornby et al. (1999) show that the magnitude of the horizontal gradient – normalized appropriately to correspond with wavelet theory – changes amplitude with upward continuation/scale-change in such a fashion as to identify the Lipschitz exponent (related to the fractal dimension) of the underlying singularity in the source distribution. That is, if we define

$$M \equiv (z/z_0) \|\overrightarrow{\partial f/\partial x} + \overrightarrow{\partial f/\partial y}\| \quad (1)$$

where f is our potential field (e.g. $f = \|g_z\|$ for gravity surveys, or $f =$ pseudogravity for magnetic surveys) then $\partial M/\partial z$ is the quantity of interest in determining the Lipschitz exponent. M is usually displayed as the worm color, and one can visually assess $\partial M/\partial z$ from the graphical representation. The Lipschitz exponent concept is closely related to the geophysically-more-widely-known ‘structural index’ from Euler deconvolution (e.g. Reid et al., 1990). An in-prep. masters thesis (Navarrete, 2015) has shown that the locations of worms and Euler solution routinely coincide, but that the worm technique offers significantly enhanced lateral coverage over the Euler deconvolution solutions.

Some practical advantages of the worm method include:

- When draped underground as in Figure 2, the worms resemble lateral contacts and reproduce (at least near the surface) the sense of dip of the contact. This provides an immediate cue towards a sensible geologic interpretation. Unfortunately – once getting beyond ‘shallow’ and ‘steep’ – the magnitude of dip is more problematic, since the field is due to more than one body and interactions between sources cause complexities. Jessell (2001) summarizes a large number of cases of worm behavior for different structural geologic settings.
- The worms commonly extend information about lateral discontinuities over large regions. This offers the geological interpreter a chance to connect structures that might not be recognized as being related.
- Deep worms tend to represent (smoothed) major lateral boundaries. By following the worm sheets upwards, the connected shallow expressions can be identified. At the scale of the GPFA, those major lateral boundaries are commonly associated with terrane boundaries or other major tectonic sources.

The worms are best visualized in 3 dimensions in order to see their interrelations. In previous efforts, that has led to working with them primarily in graphical visualization packages such as VTK (Schroeder et al., 2004) and VisIt (Childs et al., 2005) or commercial mining industry visualization packages such as FracSIS (RungePincockMinarco, 2015). For the GPFA-AB project, we need to incorporate the worms with other GIS information, but few GIS packages deal fluidly with 3D visualization. ArcScene – a component of ArcGIS – can in fact display 3D GIS information, but worms present a serious performance problem for ArcScene due to the large number of individual items that must be displayed. For the GPFA-AB project, we work around this problem by displaying worms from a restricted series of depths in 2D map view in ArcMap or QGIS, but the results are less useful than a wished-for performant 3D GIS could produce.

The worm results for the GPFA-AB project are calculated by open-source code described in Horowitz and Gaede (2014). A git repository of that code may be found at <https://bitbucket.org/fghorow/bsdwormer> with its complete revision history. Figure 3 shows worms calculated using that software from a 2.5 km resolution interpolation of the gravity Bouguer anomaly calculated from the GPFA-AB study region. The gravity station measurements were drawn both from the PACES database (Hildenbrand et al., 2002) and from a preliminary compilation filling in gravity stations in Pennsylvania (Malinconico and Moore,

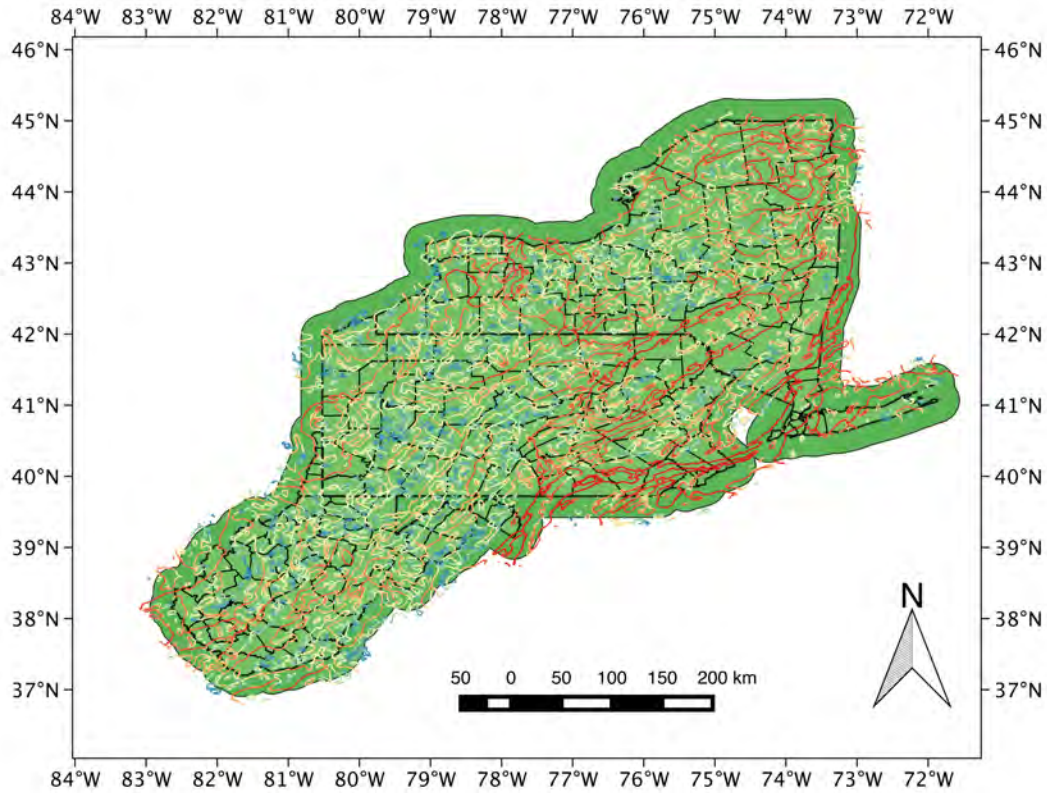


Figure 3: Displayed are gravity worms from the GPFA-AB region. The worms are from upward-continued heights (corresponding to depths as discussed above) ranging from 1 to 3 km inclusive. Each worm segment is colored according to \log_{10} of the M defined in equation (1) above. The worm color scale ranges from violet for low values of M to red for high values of M . See text for a more complete description.

2013). The preprocessing for those data – performed in the commercial software Oasis/Montaj – included selected removal of outliers and interpolation using a minimum curvature algorithm. Figure 4 shows worms calculated using that software from a 1.25 km resolution interpolation (Ravat et al., 2009) of the magnetic pseudogravity anomaly (e.g. Blakely, 1996) from the GPFA-AB study region. The pseudogravity calculation from the underlying magnetic grid was also performed in Oasis/Montaj.

Displayed in Figure 5 are locations of all earthquakes in the region retrieved from two catalogs: the US National Earthquake Information Center’s (NEIC) catalog – from 1 January 1965 through 31 May 2015, and EarthScope’s Transportable Array (TA) catalog of events from the Array Network Facility recorded during the TA’s deployment in the region (currently being removed). The date range for events from the TA are 16 March 2011 through 31 May 2015.

Importantly, the NEIC catalog, drawing on USGS seismologists’ manual efforts, identifies events that are categorized as earthquakes – as opposed to (e.g.) blasting events associated with mining or quarrying – enabling a simple database query to retrieve only earthquake events. Unfortunately, the TA catalog has no such categorization underpinning it (Astiz et al., 2014) – which resulted in my initially including events that

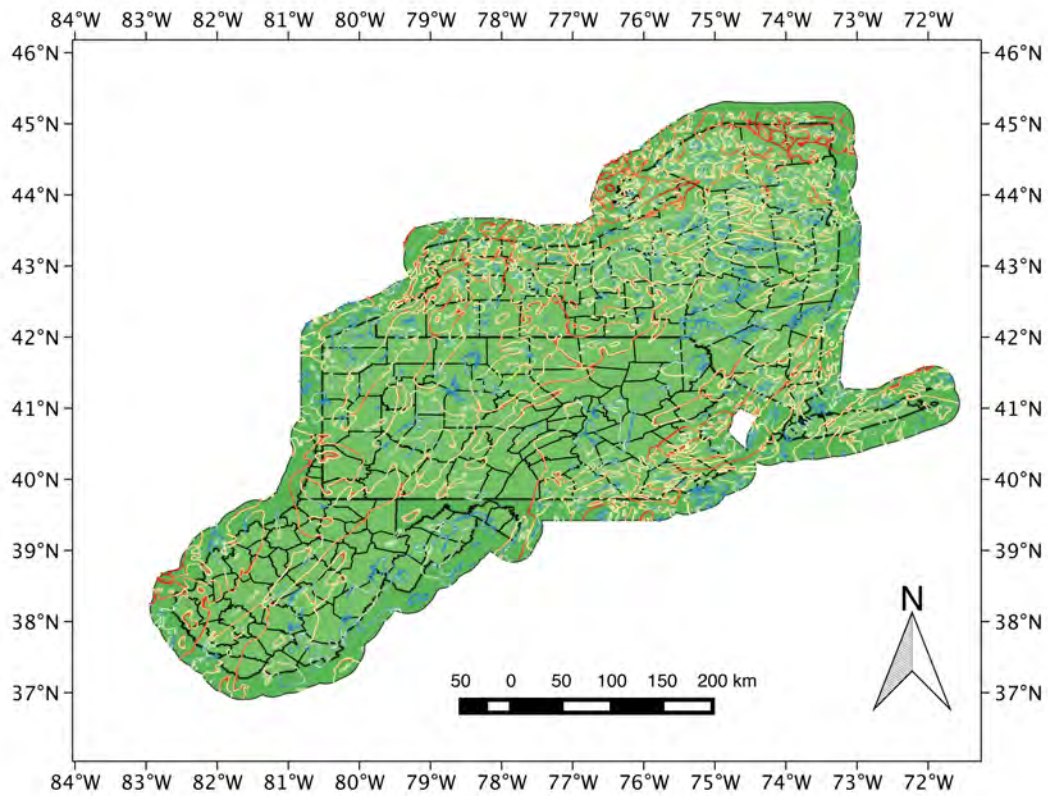


Figure 4: Displayed are magnetic worms from the GPFA-AB region. The worms are from upward-continued heights (corresponding to depths as discussed above) ranging from 1 to 3 km inclusive. Each worm segment is colored according to \log_{10} of the M defined in equation (1) above. The worm color scale ranges from violet for low values of M to red for high values of M . See text for a more complete description.

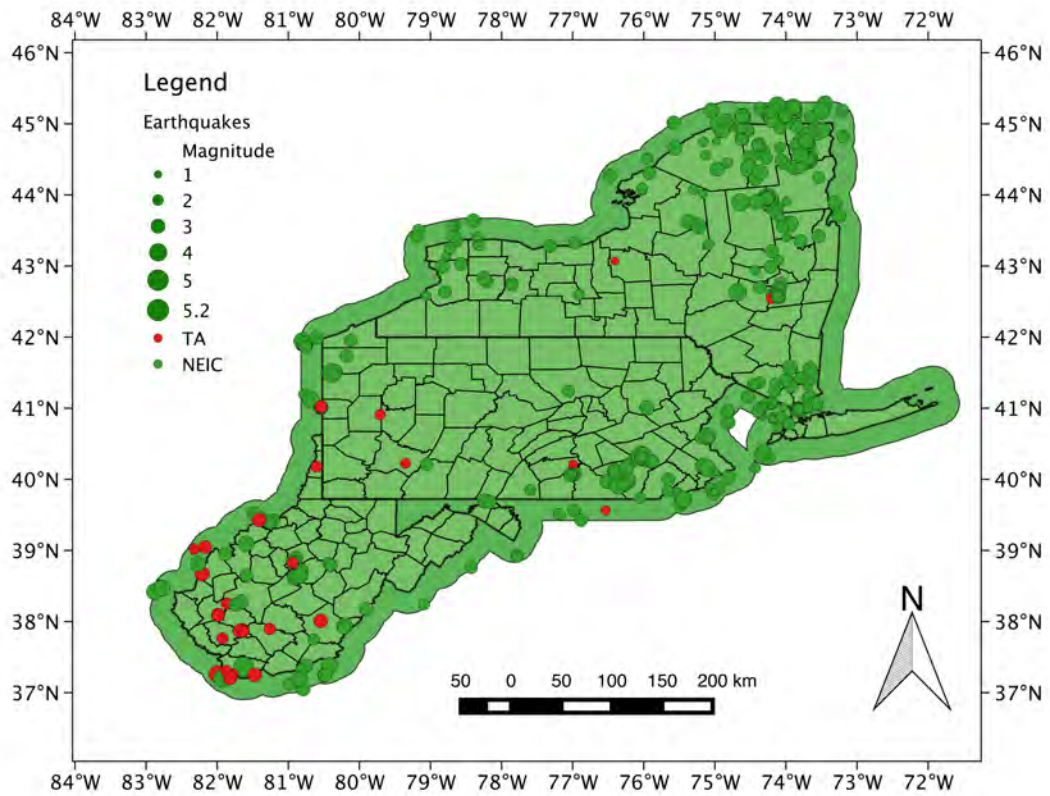


Figure 5: Displayed are earthquake epicenters from the GPFA-AB region. Shown in green are earthquake events drawn from the NEIC catalog. Shown in red are events not identified as potential blasts drawn from the TA catalog after application of the approximate de-contamination algorithm described in the text. Earthquake magnitudes M_L are displayed proportional to the radius of each event.

were almost certainly artificial blasts in the combined catalog. This was most discernible in the coal mining areas of southwest West Virginia, which appeared to have a large and active region of seismicity when plotting the raw TA data. After consultation with colleagues at the West Virginia Geological and Economic Survey drew our attention to this error, GPFA-AB investigator Beatrice Magnani of SMU suggested implementing an approximate de-contamination algorithm based on a time-of-day attribute of anthropogenic mining blasts. Quoting Astiz et al. (2014), "...mine blasting in the United States is allowed only between sunrise and sunset (Mining Safety and Health Administration, Title 30 CFR, MSHA, U.S. Department of Labor)." This led me to remove all TA events in the GPFA-AB region occurring between 07:00 and 18:00 local times. While those are only approximate local hours for sunrise and sunset, that simple algorithm removed the vast majority of TA events in the coal mining region of southwestern West Virginia – as well as some suspicious events from quarries located near to the New York State Thruway corridor and others possibly associated with shale gas hydraulic fracturing activities in regions of Pennsylvania associated with Marcellus shale development (Figure 6). Clearly, however, some natural earthquakes might also have been removed by this approximate algorithm. The odds of retaining detected natural seismicity in the TA results are only 13 in 24 because 11 hours each day were rejected. This unfortunate feature of our analysis must remain until seismologists can evaluate seismograms for the characteristics of blasts (e.g. emergent P arrivals, low amplitude S arrivals) from all 1647 TA events flagged as "daylight" in our region – deemed well beyond the scope of this study.

One method for identifying active faults was to simply find (via GIS methods) those worms which are physically close to a recorded earthquake. Under the assumption that any earthquake epicenters from sparse seismometer locations and poorly known velocity structures would yield mislocations of some distance, I felt this was an appropriate 'objective' way of identifying activated faults. Figure 7 displays a subset of those worms from figures 3 and 4 that are near to earthquakes. These structures are deemed to have an elevated risk factor for seismicity. The example distance ranges in 5 km increments shown in Figure 7 are not the actual values chosen in the combined risk factor assessment map – see that memo for details. Also, for error estimates, all earthquake locations were assumed to have 2.5 km standard deviation circles, while gravity and magnetic worm point location errors were assumed to have 500m and 250m standard deviations respectively. A clear drawback of the technique is that it only identifies structures active recently enough to have instrumentally recorded earthquakes.

After discussions with several people both inside the project and outside (including David Castillo, a former director of the oilfield borehole stability consultants Geomechanics International – now part of Baker-Hughes), it became clear that a potentially more relevant approach to estimating the risk factor for seismicity would be to determine the angle of a structure to the regional direction of the principal compressive stress (σ_1). This is supported by examination of figure 8, which shows some relevant Mohr's circles along with both Byerlee's Law (Byerlee, 1978) and Griffith-Coulomb failure envelopes. In those Mohr-space figures, two planes best oriented for failure by Byerlee's Law are marked with red dots. (There are two additional symmetrical orientations in the lower half of the Mohr diagram not shown for visual simplicity.) Those planes with normals not parallel to the principal stress directions would plot in the interstitial crescents between the circles. This leads to the conclusion that the angle a candidate plane normal makes from σ_1 is a sensitive parameter for proximity to failure under a Mohr-Coulomb failure model (Rick Allmendinger, pers. comm., 2015).

One major caveat: that orientation-in-a-regional-stress-field conclusion holds true wherever the actual state of stress is known (i.e. where the radii of the Mohr's Circles in figure 8 are established). In our situation however, we have very little information about the magnitudes of the principal stresses – other than the trivial vertical lithostatic case due to burial depth and ρgh . An unavoidable consequence of that fact is that

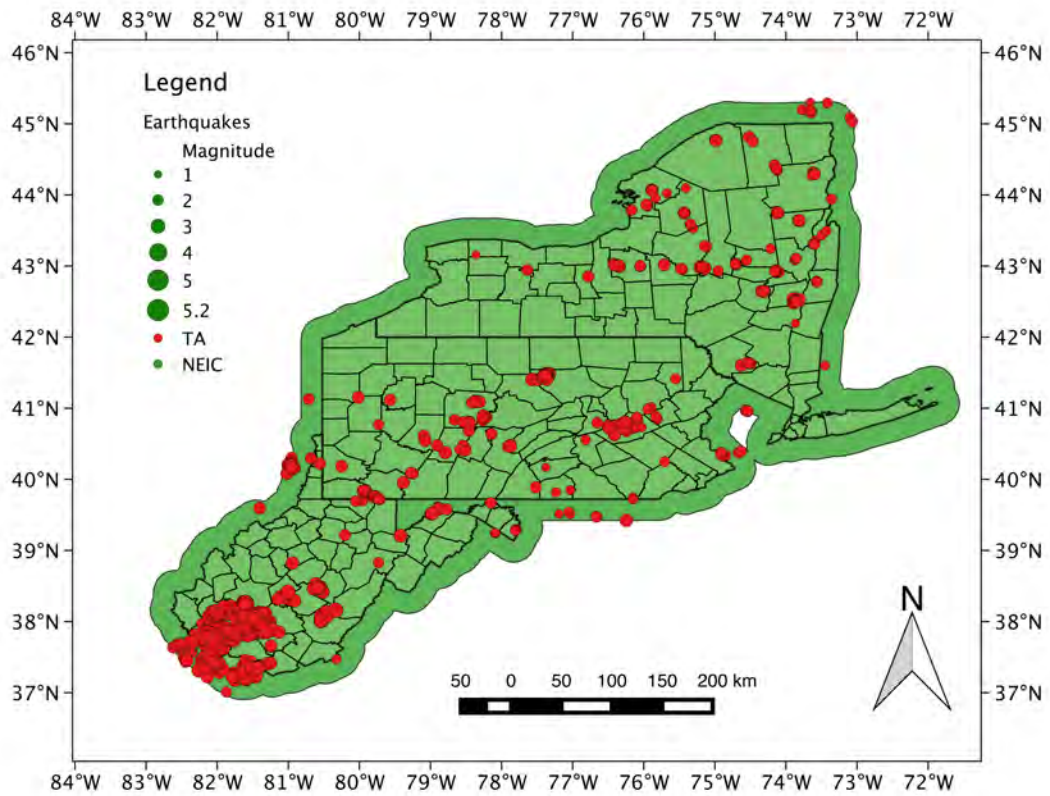


Figure 6: Displayed are suspected mining and quarry blasts from the GPFA-AB region. Shown in red are events identified as suspected mining and quarrying blasts drawn from the TA catalog after application of the approximate de-contamination algorithm described in the text. Earthquake magnitudes M_L are displayed proportional to the radius of each event.

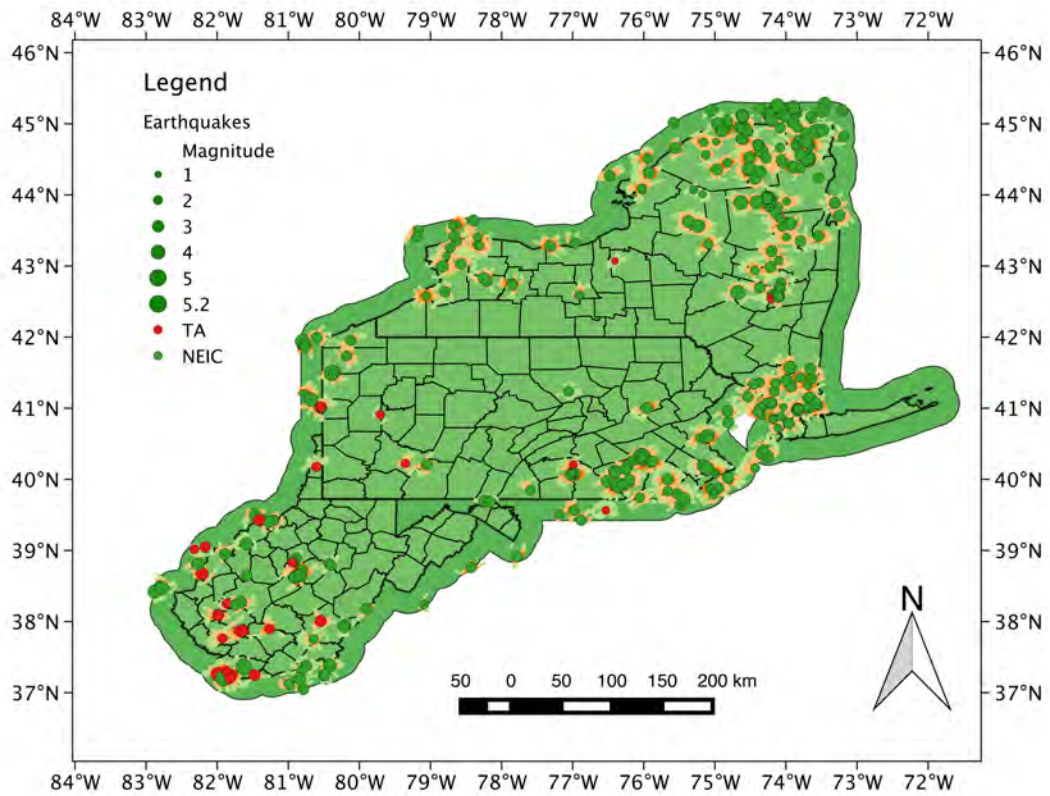
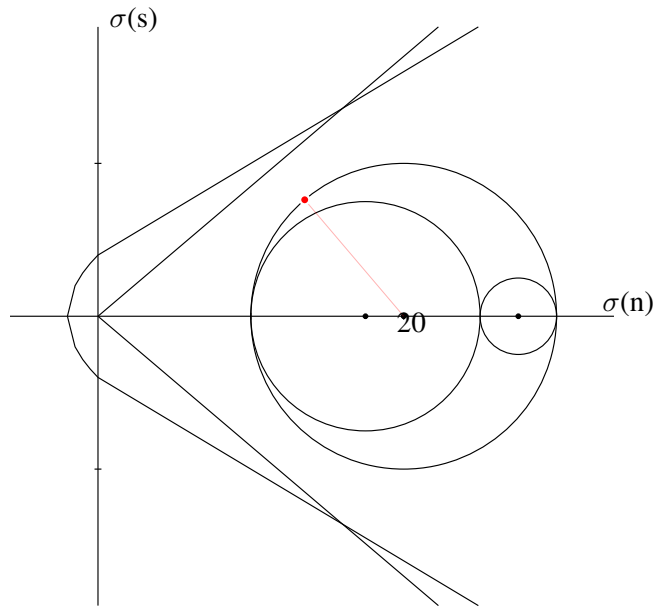
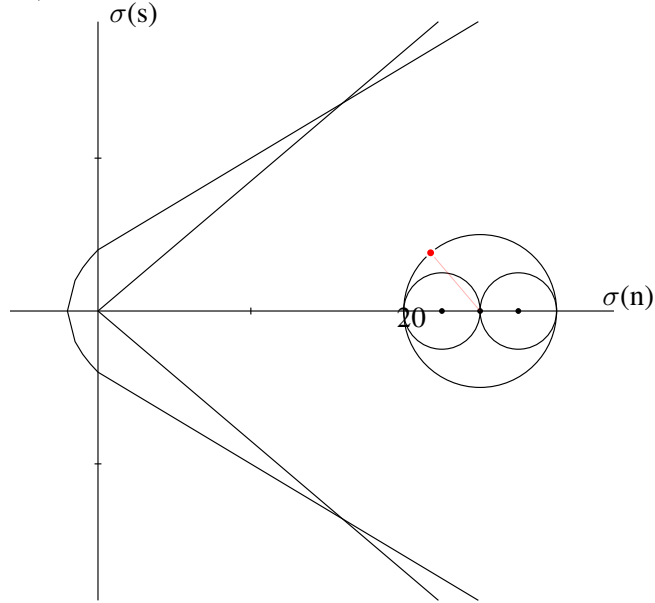


Figure 7: The subset of worms from both figures 3 and 4 that are found within specified ranges of the recorded earthquakes described in Figure 5. Shown in red are worm points within 5km of an earthquake; in orange are points between 5 and 10km; in yellow are points between 10 and 15km; and in light green are points from 15 to 20km.



(a) 3D Mohr's circles for notional principal stresses of 30, 25, and 10 MPa.



(b) 3D Mohr's circles for notional principal stresses of 30, 25, and 20 MPa.

Figure 8: Shown in (a) are 3D Mohr's circles, along with failure envelopes for both pre-existing fractures (Byerlee's Law – straight line envelope; coefficient of friction $\mu = 0.85$) and failure of intact rock (Griffith-Coulomb criterion – curved envelope). Similarly for (b), but with a different value of σ_3 resulting in a significantly further from failure situation. In both plots, the poles of the closest-to-failure planes are plotted as a red dot on the circumference of the outer (σ_1 - σ_3 plane) circle. The angles of poles to the closest-to-failure plane are identical in the two situations even though (b) is less risky than (a) because its red dot is further away from a failure envelope. Plotted using Rick Allmendinger's MohrPlotter software.

any risk estimates we make using this technique are *local only*. Local changes in risk nearby along worm segments should be qualitatively captured – assuming locally smooth changes in stress magnitudes. However, quantitatively comparing the seismic risk factor from one location to another location at some distance removed is not feasible because the unknown stress magnitudes also play a role not captured by orientation. Hence, segments identified as possessing the same ‘risk factor’ using this technique will unavoidably have different quantitative risks of seismicity. Another way of saying the same thing is that planes with poles nearly normal to the Byerlee’s Law envelope in both figures 8a and 8b, will be estimated to have the same risk using this technique, even though the situation in figure 8a is significantly closer to failure.

An alternative take on these drawbacks focusing more on *induced* seismicity in a geothermal field – and due originally to Katie Keranen and Terry Jordan – is as follows:

...It is unavoidable that the products of the Phase 1 analysis at the regional scale are of low reliability as indicators of the risk of induced seismicity for two reasons. First, some of the critical information used to predict rock failure is only available by use of long distance extrapolation of sparse data points. Second, the local details of rocks, fluids, and stresses are not merely down-scaled samples of the regional tendencies. Instead, local details produce field-specific conditions of stress and of failure even in the unlikely situation that the population of fault orientations happens to be alike in two different fields, and even if the production/injection fluid pressure design is equal in two different fields.

I turn the orientation-in-a-regional-stress-field sensitivity conclusion into a practical method for determining a quantitative index of seismic risk (and its error) via the the following procedures. Figure 9 shows the relevant geometry for estimating worm orientation and error at each worm point. The worm azimuth at node n_i is estimated as α_i^s , and the normal to that direction is the unit vector ν_i . The circular error variance of both α_i^s and ν_i is computed as follows. Briefly, if one half of the magnitude of the vector sum of unit vectors in the α_i and α_{i+1} directions is defined as \bar{R} , the circular variance (S_0) is defined as $1 - \bar{R}$ (Mardia, 1972, Eq. 2.3.5). That procedure establishes the local worm orientation, its normal unit vector (under an approximation of vertical dip), and provides an estimate of error for those quantities. Hence, via that procedure all required quantities are assigned to nodes rather than edges.

Next, I turn to estimating the orientation of the regional stress field from the World Stress Map (WSM) project (Heidbach et al., 2010). Figure 10 shows the locations of both the primary observations of σ_1 orientations (in red), and the result of a smoothing algorithm that plots the orientations on a 0.5 degree of arc grid (in black). Briefly, the WSM smoothing algorithm weights observed stress orientations by quality, then at each candidate point where an interpolation is to be estimated it collects all observations within a 1000 km radius. If there are more than 5 observations included, it continues, otherwise it stops, “censors” that point from the interpolation, and moves on to the next candidate interpolation point. If a candidate interpolation point is still valid, the algorithm additionally weights those observations by the inverse of the distance between an observation and the interpolation point (to a minimum allowed distance of 20 km), takes those exact quantities, and performs a Mardia (1972) style average direction and error estimate. If the standard deviation is less than 25° , the procedure stops and those average orientations and error estimates are used. If, however, the standard deviation is greater than 25° , the algorithm reduces the search radius by 100 km, and repeats itself down to a minimum search radius of 100 km. Thus, there are 2 separate ways in which a point can be “censored” from an interpolation: by having fewer than 5 observations within a search radius, or never finding a standard deviation of less than 25° for all search radii down to 100 km.

Heidbach et al. (2010) cite Mardia (1972) as the origination of the quality and inverse-distance weighted spatial interpolation algorithm they use. I believe that is inaccurate – because one of Mardia’s

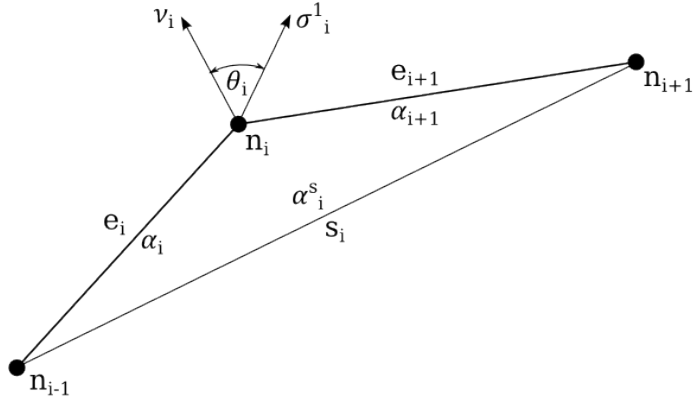


Figure 9: Map view of the relevant geometry of worm segments in a regional stress field. Displayed with labels n and e are nodes and edges (respectively) of the worm segments computed by the code described by Horowitz and Gaede (2014). All subscripts in this figure denote indices for consecutive elements of worm geometry components. The angles α_i denote the azimuthal (strike) angles for the corresponding segments e_i . The so-called secant line between nodes n_{i+1} and n_{i-1} is labeled s_i , and its azimuthal strike angle is labeled α_i^s . That azimuth α_i^s is assigned to node n_i , as is the orientation of a unit vector normal to s_i denoted here as ν_i . Also shown at node n_i is a unit vector in the direction of the maximum principal compressive stress σ_i^1 . The angle θ_i between ν_i and σ_i^1 is the primary risk index for point n_i under this approach. The analysis described here and in the text is repeated for all worm nodes except for those at the ends of individual worm segments – where angle variances are ill-defined. See the text for more discussion on why these quantities were selected.

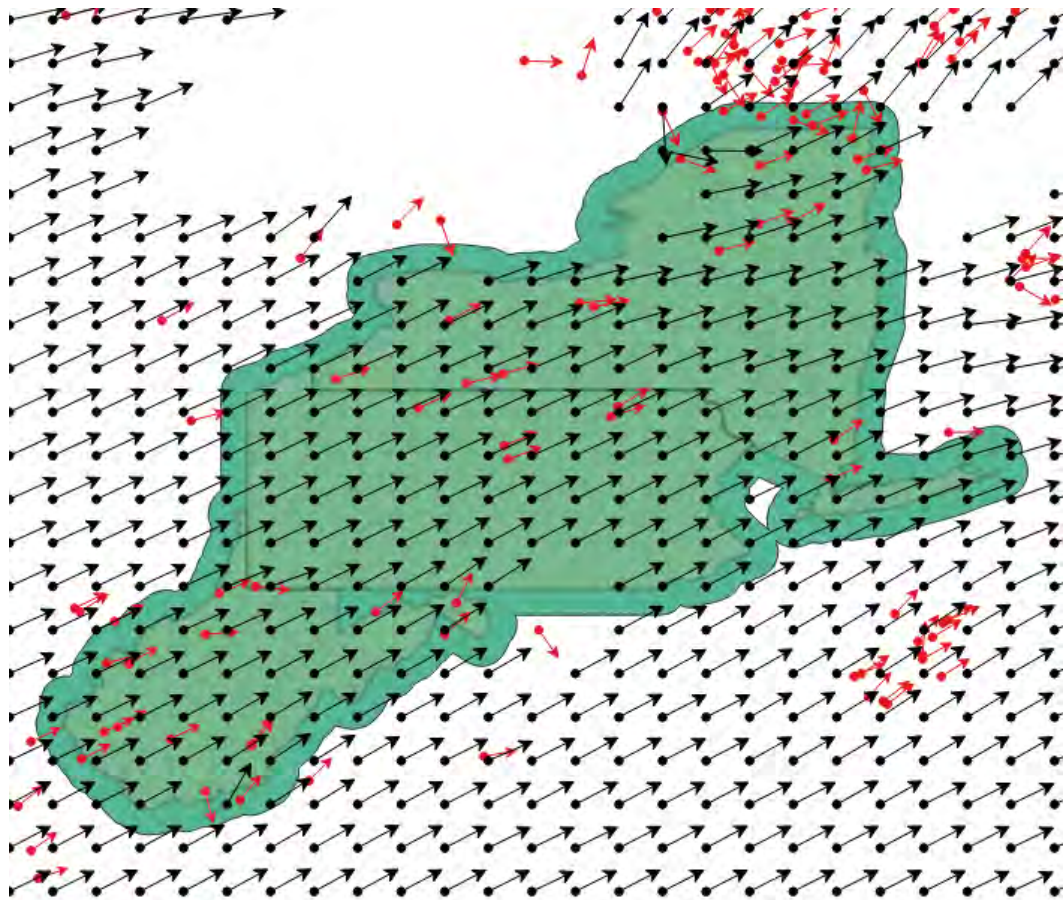


Figure 10: Principal compressive stress (σ_1) directions from the World Stress Map (WSM: Heidbach et al., 2010). Plotted in red are all regional primary observations from the WSM drawn from their quality ratings of A,B, or C. Plotted in black are their smoothed results. The smoothed directional field is evaluated on gridpoints of spacing 0.5 degrees of arc, using a censoring procedure also described in their paper. Gaps in the smoothed (black) field result from that decimation.

key concepts is to always work on the unit circle, which is violated by weighting the vector lengths as described above. Additionally, Mardia (1972) does not contain any mention of spatial interpolations – that I was able to find at least. Hence, for better or worse, I attribute that algorithm to Heidbach et al. (2010). I perform the algorithm just described to estimate the regional stress orientation and the associated angular error at the position of each worm point.

The final component of the orientation-in-stress-field risk estimation procedure is to calculate the angle between the σ_1 direction and the worm segment normal direction, and to compare that angle with the angular values most favored for failure in Figure 8. For the depth ranges appropriate for this work, the normal stresses are likely to be below 200 MPa and thus Byerlee’s Law (Byerlee, 1978) claims a coefficient of friction of $\mu = 0.85$ as appropriate for a broad range of rock types. I adopt that value here.

For reference, converting that coefficient of friction value to the angular orientation of the normals ideally oriented for failure by Byerlee’s law (the red lines in Figure 8) proceeds as follows. Denoting θ_B as the Mohr space angle between the Byerlee failure envelope and the σ_1 direction, examination of the relevant geometry implies that $\theta_B = \tan^{-1}(\mu) \approx 40.4^\circ$. Hence, the complement of θ_B is about 49.6° , and the supplement of that ($\approx 130.4^\circ$) is the Mohr-space angular deviation from the σ_1 direction of the highest-risk orientation. Accordingly, by the properties of the Mohr diagram construction, the critical angle in real-space is $\theta_{crit} \approx 130.4^\circ/2 = 65.2^\circ$. There is another critical orientation with the opposite sense (not plotted for visual simplicity) in Figure 8. The end result is that there are two critical angular deviations from the σ_1 direction, $\theta_{crit} = \pm 65.2^\circ$.

Thus, I establish angular risk categorization for this orientation-in-stress-field analysis by identifying arcs of orientations of \pm a specified angular range around both sides of both critical orientations. Figure 11 illustrates that technique for ranges increasing by 5° between risk categories.

Once again, the specific break values in risk categorization discussed here may not be the final categorization used in the overall risk-factor merging process. Please consult that separate memo for details.

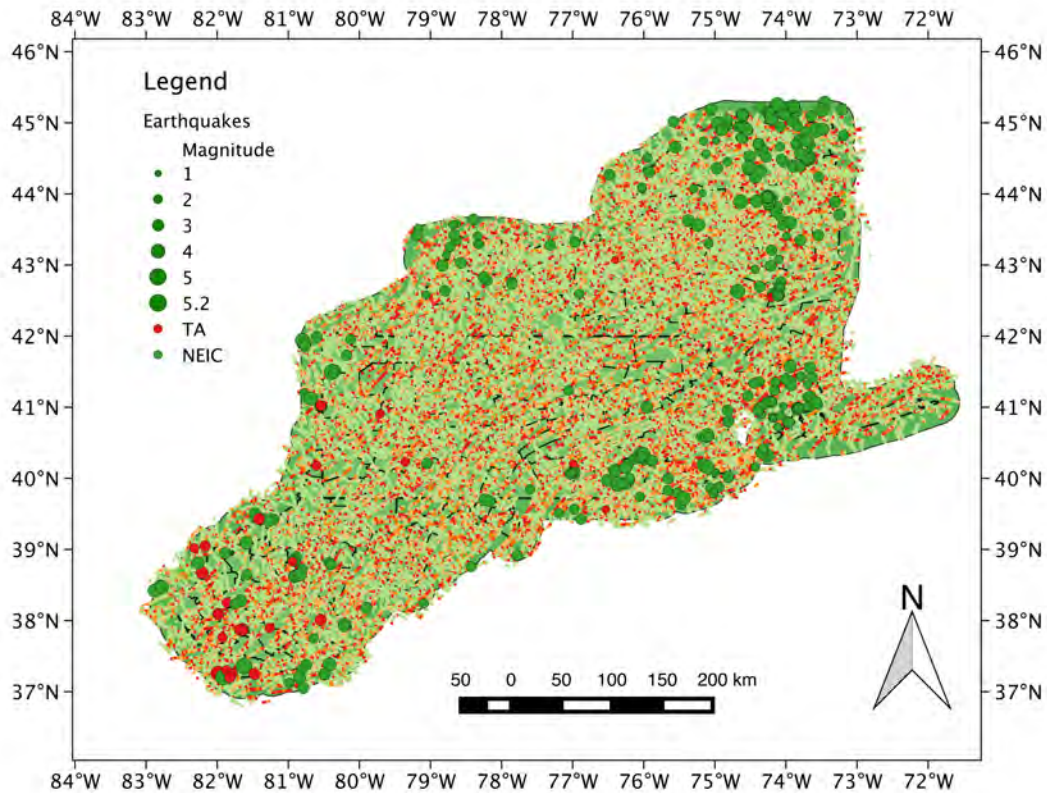


Figure 11: Worms combined from both figures 3 and 4 showing relative risks due to orientation in the estimated regional stress field. Points are colored red for the case where worm segments are within 5° on both sides of the θ_{crit} values; orange for an additional 5° arc outside the red range; yellow for an additional 5° arc outside the orange range; and light green for all positions on structures oriented outside the yellow range. In this classification, all points on structures identified by worms have slightly elevated (“moderately low”/light green) risks of seismicity simply due to the fact that they are on identified geological structures – which are heterogeneities that might localize stresses. Points not on worms are assigned to the “low-risk” category, and are not explicitly plotted in this figure. Also not shown in this figure are the error estimates calculated from the procedure discussed in the text – although both the relative orientation and error values were incorporated into the combined risk estimate phase of the GPFA-AB project.

References

- Astiz, L., Eakins, J. A., Martynov, V. G., Cox, T. A., Tytell, J., Reyes, J. C., Newman, R. L., Karasu, G. H., Mulder, T., White, M., Davis, G. A., Busby, R. W., Hafner, K., Meyer, J. C., and Vernon, F. L. (2014). The Array Network Facility Seismic Bulletin: Products and an Unbiased View of United States Seismicity. *Seismological Research Letters*, 85(3):576–593. Available from: <http://dx.doi.org/10.1785/0220130141>.
- Blakely, R. J. (1996). *Potential Theory in Gravity and Magnetic Applications*. Cambridge University Press, Cambridge. Available from: <http://dx.doi.org/10.1017/CBO9780511549816>.
- Boschetti, F., Hornby, P., and Horowitz, F. G. (2001). Wavelet Based Inversion of Gravity Data. *Exploration Geophysics*, 32,(1):48–55. Available from: <http://dx.doi.org/10.1071/EG01048>.
- Byerlee, J. (1978). Friction of rocks. *Pure and Applied Geophysics*, 116(4-5):615–626. Available from: <http://dx.doi.org/10.1007/bf00876528>.
- Childs, H., Brugger, E. S., Bonnell, K. S., Meredith, J. S., Miller, M., Whitlock, B. J., and Max, N. (2005). A Contract-Based system for large data visualization. In *Proceedings of IEEE Visualization 2005*, pages 190–198. Available from: <http://visit.llnl.gov/>.
- GoldCorp (2001). US\$575,000 Goldcorp Challenge Awards world's first 6 million ounce internet gold rush yields high grade results! Press Release. Available from: <http://www.infomine.com/index/pr/Pa065434.PDF>.
- Heidbach, O., Tingay, M., Barth, A., Reinecker, J., Kurfeß, D., and Müller, B. (2010). Global crustal stress pattern based on the World Stress Map database release 2008. *Tectonophysics*, 482(1-4):3–15. Available from: <http://dx.doi.org/10.1016/j.tecto.2009.07.023>.
- Hildenbrand, T. G., Briesacher, A., Flanagan, G., Hinze, W. J., Hittelman, A. M., Keller, G. R., Kucks, R. P., Plouff, D., Roest, W., Seeley, J., Smith, D. A., and Webring, M. (2002). *Rationale and Operational Plan to Upgrade the U.S. Gravity Database*. Number 02-463 in USGS Open File Report. Available from: <http://research.utep.edu/default.aspx?tabid=37229>.
- Hornby, P., Boschetti, F., and Horowitz, F. G. (1999). Analysis of potential field data in the wavelet domain. *Geophysical Journal International*, 137(1):175–196. Available from: <http://dx.doi.org/10.1046/j.1365-246x.1999.00788.x>.
- Hornby, P., Horowitz, F. G., and Boschetti, F. (2002). A physical interpretation of the Poisson wavelet transform of potential fields. In *Proceedings, EGS XXVII General Assembly, Munich*. European Geophysical

- Society, European Geophysical Society. Available from: <http://www.cosis.net/abstracts/EGS02/05568/EGS02-A-05568.pdf>.
- Horowitz, F. G. and Gaede, O. (2014). BSDWormer; an open source implementation of a Poisson wavelet multiscale analysis for potential fields. In *2014 Fall Meeting*, number T43C-4743. American Geophysical Union. Available from: <https://agu.confex.com/agu/fm14/meetingapp.cgi\#Paper/26847>.
- Jessell, M. (2001). An atlas of structural geophysics II. *Journal of the Virtual Explorer*, 05. Available from: <http://virtualexplorer.com.au/journal/2001/05>.
- Malinconico, L. and Moore, M. (2013). Provisional Bouguer gravity map of Pennsylvania. AASG Geothermal Data Repository. Available from: <http://repository.stategeothermaldata.org/repository/resource/a748ce233a25e3e0dd00c9865d0af3e5/>.
- Mallat, S. and Zhong, S. (1992). Characterization of signals from multiscale edges. *Pattern Analysis and Machine Intelligence, IEEE Transactions on*, 14(7):710–732. Available from: <http://dx.doi.org/10.1109/34.142909>.
- Mardia, K. V. (1972). *Statistics of directional data*. Academic Press. Available from: <http://www.worldcat.org/isbn/9780124711501>.
- Moreau, F., Gibert, D., Holschneider, M., and Saracco, G. (1997). Wavelet Analysis of Potential Fields. *Inverse Problems*, 13:165–178. Available from: <http://dx.doi.org/10.1088/0266-5611/13/1/013>.
- Navarrete, L. (2015). Crustal structure of NE N America from constrained models of potential field data. Master's thesis, University of Rochester.
- Ravat, D., Finn, C., Hill, P., Kucks, R., Phillips, J., Blakely, R., Bouligand, C., Sabaka, T., Elshayat, A., Aref, A., and Elawadi, E. (2009). *A Preliminary, Full Spectrum, Magnetic Anomaly Grid of the United States with Improved Long Wavelengths for Studying Continental Dynamics: A Website for Distribution of Data*. Number Open-File Report 20091258. USGS. Available from: <http://pubs.usgs.gov/of/2009/1258/>.
- Reid, A. B., Allsop, J. M., Granser, H., Millett, A. J., and Somerton, I. W. (1990). Magnetic interpretation in three dimensions using Euler deconvolution. *GEOPHYSICS*, 55(1):80–91. Available from: <http://dx.doi.org/10.1190/1.1442774>.
- RungePincockMinarco (2015). Data Integration and 3d Visualisation Software - FRACIS. webpage retrieved 23 June 2015. Available from: <http://www.rpmglobal.com/mining-software/data-visualisation-fracsis>.
- Schroeder, W., Martin, K., and Lorensen, B. (2004). *The Visualization Toolkit*. Kitware Inc., third edition. Available from: <http://www.worldcat.org/isbn/1930934122>.

Acknowledgements

I thank David Castillo, Katie Keranen, Rick Allmendinger, and Geoff Abers for suggesting that I use orientation in a regional stress field as a method of determining the risk of seismicity on a structure. I thank Ronald McDowell and others from the West Virginian Geological and Economic Survey for calling to our attention that we had mine blasts contaminating our TA seismic catalog information, and I thank Beatrice Magnani of SMU for suggesting the statistically viable decontamination method of removing daylight events. I also thank Jery Stedinger for keeping me honest about determining quantitative errors in my risk estimates.